INTERNATIONAL JOURNAL FOR NUMERICAL METHODS IN FLUIDS, VOL. 21, 735–761 (1995)

FLUID DYNAMICS OF SLENDER, THIN, ANNULAR LIQUID JETS

J. I. RAMOS

Departamento de Lenguajes y Ciencias de la Computación, E. T. S. Ingenieros Industriales, Universidad de Málaga, Plaza El Ejido, s/n, 29013-Málaga, Spain

SUMMARY

Perturbation methods are used to obtain the one-dimensional, asymptotic equations that govern the fluid dynamics of slender, thin, inviscid, incompressible, axisymmetric, irrotational, annular liquid jets from the Euler equations. It is shown that, depending on the magnitude of the Weber number, two flow regimes are possible: an inertia-dominated one corresponding to large Weber numbers, and a capillary regime for Weber numbers of the order of unity. The steady equations governing these two regimes have analytical solutions for the liquid's axial velocity component and require a numerical integration to determine the jet's mean radius for inertia-dominated jets. The one-dimensional equations derived in this paper are shown to be particular cases of a hydraulic model for annular liquid jets, and this model is used to determine the effects of gravity modulation on the unsteady fluid dynamics of annular liquid jets in the absence of mass injection into the volume enclosed by the jet and mass absorption. It is shown that both the convergence length and the pressure coefficient are periodic functions of time which have the same period as that of the gravity modulation, but undergo large variations as the amplitude, frequency and width of gravitational pulses is varied.

KEY WORDS: perturbation methods; adaptive finite differences; annular liquid jets; one-dimensional models; gravity modulation

1. INTRODUCTION

The fluid dynamics of annular liquid jets dates back to Boussinesq,[1,2] who developed a one-dimensional, steady model based on the application of Newton's second law to a differential control volume of the jet. His model also assumed that the pressure is uniform throughout the liquid and that the velocity components are not functions of the radial co-ordinate. Boussinesq[1,2] also used co-ordinates along and normal to the jet's mean radius. Boussinesq's model is strictly valid for thin, annular liquid jets, and has been employed by Lance and Perry,[3] Hopwood[4] and Taylor,[5] and Baird and Davidson,[6] Binnie and Squire[7] and Dumbleton[8] to analyse the steady fluid dynamics of water bells and annular liquid jets, respectively.

The equations derived by Boussinesq[1,2] were projected onto a cylindrical, polar co-ordinate system by Hoffman *et al.*[9] and Ramos.[10] The latter also obtained analytical solutions for long jets, i.e. jets whose mean radius at the nozzle exit is much smaller than the distance from the nozzle exit to the axial location at which the annular jet becomes a solid one (cf. Figure 1). This distance is here referred to as the convergence length.

Lee and Wang[11,12] developed a Lagrangian model for unsteady, annular liquid membranes, i.e. annular liquid jets of zero thickness, based on the kinematics of the membrane and the conservation of mass and linear momentum. Their model was used to study the capillary instabilities of annular membranes which result in the formation of hollow liquid shells in zero-gravity. Since a membrane has

CCC 0271–2091/95/090735–27

Received March 1995
Revised April 1995

zero thickness, it cannot stand pressure differences along it; therefore, the pressure in the model of Lee and Wang is uniform throughout the liquid.

An unsteady model of thin, annular liquid jets was derived by Ramos[13] who integrated the continuity and Euler equations along the jet's thickness, applied the kinematic and dynamic boundary conditions at the jet's interfaces (where the normal velocity component is continuous while the pressure jump at the interfaces is balanced by surface tension) and assumed that the axial and radial velocity components are uniform at each cross-section of the jet. Also, the pressure was assumed uniform throughout the liquid. The hydraulic model of Reference 13 reduces to that of Boussinesq[1,2] for steady and long, annular jets. Although the model of Reference 13 has produced good agreement with experimental data,[14] the assumptions of uniform pressure throughout the jet, and axial and radial velocity components independent of the radial co-ordinate may not be justified.

In this paper, the fluid dynamics of both steady and unsteady, inviscid, irrotational, incompressible, axisymmetric, thin, slender, annular liquid jets is analysed by means of perturbation methods based on the jet's slenderness and thickness ratios. (The slenderness ratio is defined as the ratio of the jet's mean radius at the nozzle exit to a characteristic axial distance, while the thickness ratio is the ratio of the jet's thickness to the mean radius at the nozzle exit.) The analysis presented in this paper is a long-wave expansion valid for long annular liquid jets of small thickness and considers surface tension at the jet's interfaces and gravity.

Depending on the magnitude of the Weber number, i.e. the ratio of inertia to surface tension, the dynamics of annular liquid jets may be controlled by inertia or capillarity. Inertia- and capillarity-dominated annular liquid jets are considered in Sections 2 and 3 respectively. The solutions to the steady equations that govern these two regimes are obtained analytically and numerically for capillarity- and inertia-dominated annular liquid jets in Section 4. Perturbation methods are also used in Section 5 to analyse the equations of the hydraulic model presented in Reference 13 and its relationship with the one-dimensional, asymptotic models of thin, slender, annular liquid jets developed in Sections 2 and 3. Some examples illustrating the shape of steady, downward and upward jets, and the unsteady fluid dynamics of annular jets subject to gravity modulation are presented in Section 7. The shape of steady, inertia-dominated, annular liquid jets has been determined by means of a fourth-order accurate Runge–Kutta method, while the effects of gravity modulation have been assessed by means of the adaptive finite-difference method of Reference 15.

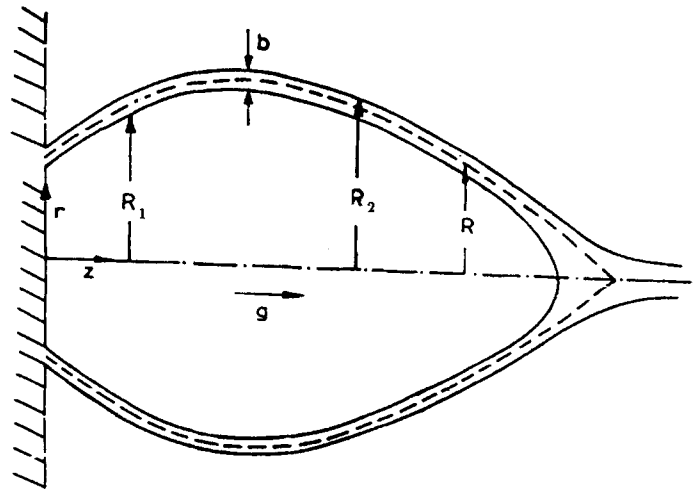

Figure 1. Schematic of a downward, annular liquid jet

2. ASYMPTOTIC ANALYSIS OF SLENDER, ANNULAR LIQUID JETS

The fluid dynamics of unsteady, axisymmetric, incompressible (constant density), inviscid, irrotational, annular liquid jets is governed by the velocity potential, ϕ^*, which satisfies the Laplace equation, i.e.

$$\frac{\partial^2\phi^*}{\partial z^{*2}}+\frac{1}{r^*}\frac{\partial}{\partial r^*}\left(r^*\frac{\partial\phi^*}{\partial r^*}\right)=0, \tag{1}$$

where the asterisk denotes dimensional quantities, and r^* and z^* are the radial and axial coordinates, respectively.

Equation (1) is subject to the following kinematic and dynamic boundary conditions at the annular liquid jet's interfaces

$$\frac{\partial\phi^*(R_i^*,z^*,t^*)}{\partial r^*}=\frac{\partial\phi^*(R_i^*,z^*,t^*)}{\partial t^*}+\frac{\partial\phi^*(R_i^*,z^*,t^*)}{\partial z^*}\frac{\partial R_i^*}{\partial z^*},\quad i=1,2, \tag{2}$$

$$p_1^*-p^*(R_1^*,z^*,t^*)=\sigma^*\left(\frac{1}{R_1^*(1+(\partial R_1^*/\partial z^*)^2)^{1/2}}-\frac{\partial^2R_1^*/\partial z^{*2}}{(1+(\partial R_1^*/\partial z^*)^2)^{3/2}}\right), \tag{3}$$

$$p^*(R_2^*(z^*),z^*,t^*)-p_2^*=\sigma^*\left(\frac{1}{R_2^*(1+(\partial R_2^*/\partial z^*)^2)^{1/2}}-\frac{\partial^2R_2^*/\partial z^{*2}}{(1+(\partial R_2^*/\partial z^*)^2)^{3/2}}\right), \tag{4}$$

where R_1^* and R_2^* are the radii of the jet's inner and outer interfaces, respectively, p^* is the pressure, σ^* is the liquid's surface tension, t^* is time, and p_1^* and p_2^* denote the pressure of the gases enclosed by and surrounding, respectively, the annular liquid jet.

The gases enclosed by and surrounding the annular liquid jet will be assumed to be dynamically passive, i.e., p_1^* and p_2^* will be assumed to be spatially uniform, since their density is, in general, much smaller than that of liquids.

In addition, initial conditions and boundary conditions at $z^*=0$, i.e. at the nozzle exit, are to be provided. The boundary conditions must be obtained by matching the potential flow inside the nozzle with that of the free, annular jet. Since the flow inside the nozzle must satisfy the no-penetration condition at the solid walls, whereas the boundary conditions for the free, annular jet involve free surfaces, a transition from the no-penetration to the free-surface flow is expected. Such a transition is not considered in this paper where the interest lies in the region below the nozzle exit.

Since the flow is irrotational, the liquid pressure can be determined from Bernoulli's equation as

$$p^*=-\rho^*\frac{\partial\phi^*}{\partial t^*}-\frac{1}{2}\rho^*\left(\left(\frac{\partial\phi^*}{\partial r^*}\right)^2+\left(\frac{\partial\phi^*}{\partial z^*}\right)^2\right)+\rho^*g^*z^*+B^*(t^*), \tag{5}$$

where ρ^* is the liquid's density, g^* is the gravitational acceleration, and B^* is the time-dependent Bernoulli constant. This constant can be included without loss of generality in the velocity potential since the velocity field is the gradient of the velocity potential and only the pressure gradient appears in the Euler equations. Note that, if this is done, p^* represents the difference between the static and stagnation pressures under steady state conditions.

For thin and slender annular liquid jets $\lambda=b_0^*/R_0^*\ll 1$ and $\varepsilon=R_0^*/L^*\ll 1$, where b_0^*, R_0^* and L^* denote the jet's thickness and mean radius at the nozzle exit and a characteristic axial distance or wave length, e.g. the convergence length, respectively. In this paper, it will be assumed that $\lambda=\varepsilon^2$. Note that $\lambda=0$ corresponds to an annular liquid membrane.

If the radial and axial co-ordinates are non-dimensionalized with respect to R_0^* and L^*, respectively, the velocity potential with respect to $u_0^* L^*$, t^* with respect to L^*/u_0^*, and the pressure with respect to $\rho^* u_0^{*2}$, where u_0^* is a (constant) reference axial velocity component, e.g. the axial velocity component at the nozzle exit, equations (1)–(5) become, after substituting (5) into (3) and (4),

$$\varepsilon^2 \frac{\partial^2 \phi}{\partial z^2} + \frac{1}{r}\frac{\partial}{\partial r}\left(r\frac{\partial \phi}{\partial r}\right) = 0, \tag{6}$$

$$\frac{\partial \phi(R_i, z, t)}{\partial r} = \varepsilon^2 \left(\frac{\partial R_i}{\partial t} + \frac{\partial \phi(R_i, z, t)}{\partial z}\frac{\partial R_i}{\partial z}\right), \quad i = 1, 2, \tag{7}$$

$$\left(\frac{\partial \phi(R_1, z, t)}{\partial r}\right)^2 = \varepsilon^2 \left(-\gamma_1 - 2\frac{\partial \phi(R_1, z, t)}{\partial t} - \left(\frac{\partial \phi(R_1, z, t)}{\partial z}\right)^2 + \frac{z}{Fr} + \frac{1}{We}\left(\frac{1}{R_1(1 + \varepsilon^2(\partial R_1/\partial z)^2)^{1/2}} - \frac{\varepsilon^2(\partial^2 R_1/\partial z^2)}{(1 + \varepsilon^2(\partial R_1/\partial z)^2)^{3/2}}\right)\right), \tag{8}$$

$$\left(\frac{\partial \phi(R_2, z, t)}{\partial r}\right)^2 = \varepsilon^2 \left(-\gamma_2 - 2\frac{\partial \phi(R_2, z, t)}{\partial t} - \left(\frac{\partial \phi(R_2, z, t)}{\partial z}\right)^2 + \frac{z}{Fr} + \frac{1}{We}\left(\frac{1}{R_2(1 + \varepsilon^2(\partial R_2/\partial z)^2)^{1/2}} - \frac{\varepsilon^2(\partial^2 R_2/\partial z^2)}{(1 + \varepsilon^2(\partial R_2/\partial z)^2)^{3/2}}\right)\right), \tag{9}$$

$$p = -2\frac{\partial \phi}{\partial t} - \left(\frac{1}{\varepsilon^2}\left(\frac{\partial \phi}{\partial r}\right)^2 + \left(\frac{\partial \phi}{\partial z}\right)^2\right) + \frac{z}{Fr}, \tag{10}$$

where $\gamma_i = 2p_i^*/\rho^* u_0^{*2}$, $Fr = u_0^{*2}/2g^* L^*$ is the Froude number, and $We = \rho^* R_0^* u_0^{*2}/2\sigma^*$ is the Weber number.

The length used to non-dimensionalize the axial co-ordinate in this section may be replaced by $u_0^{*2}/2g^*$ which corresponds to a Froude number equal to one, and the condition of slenderness implies that $u_0^{*2}/2g^* \gg R_0^*$.

Equations (6)–(10) indicate that the fluid dynamics of slender, thin, inviscid, incompressible, irotational, annular liquid jets depends on the slenderness ratio, ε, and the Froude and Weber numbers. Depending on the magnitude of these non-dimensional numbers, several flow regimes are possible: the inertia-dominated and the surface-tension dominated regimes which are analysed in Sections 2.1–2.5 and Sections 2.6 and 2.7, respectively. The inertia-dominated regime corresponds to small surface tension, while the capillary regime corresponds to large surface tension. The surface-tension dominated regime is also analysed in Section 3 using a different non-dimensionalization than the one used below.

2.1. $We = \infty$ and $Fr = O(1)$

If there is no surface tension, i.e. the Weber number is infinite, and $Fr = O(1)$, the velocity potential and the jet's mean radius at the inner and outer interfaces can be written in terms of ε^2 as

$$\phi = \phi_0 + \varepsilon^2 \phi_2 + O(\varepsilon^4), \tag{11}$$

$$R_1 = R_0 + \varepsilon^2 R_{12} + O(\varepsilon^4), \tag{12}$$

$$R_2 = R_0 + \varepsilon^2 R_{22} + O(\varepsilon^4). \tag{13}$$

Note that the jet's thickness which has been non-dimensionalized with respect to R_0^*, may be written as

$$b = R_2 - R_1 = \varepsilon^2 b_2 + O(\varepsilon^4), \tag{14}$$

where

$$b_2 = R_{22} - R_{12}, \tag{15}$$

which implies that the volumetric flow rate at the nozzle exit is $O(\varepsilon^2)$.

Expansion of the kinematic (equation (7)) and dynamic (equations (8) and (9)) boundary conditions at R_1 and R_2 in Taylor's series around R_0, i.e. the jet's mean radius, and substitution of (11)–(13) into (6)–(9) result in a system of equations in powers of ε^2. Equating terms of $O(\varepsilon^0)$ yields

$$\frac{1}{r}\frac{\partial}{\partial r}\left(r\frac{\partial \phi_0}{\partial r}\right) = 0, \tag{16}$$

$$\frac{\partial \phi_0(R_0, z, t)}{\partial r} = 0, \tag{17}$$

The solution of (16) subject to (17) is $\phi_0(r, z, t) = B(z, t)$.

Equating terms of $O(\varepsilon^2)$ yields

$$\frac{\partial^2 \phi_0}{\partial z^2} + \frac{1}{r}\frac{\partial}{\partial r}\left(r\frac{\partial \phi_2}{\partial r}\right) = 0, \tag{18}$$

$$\frac{\partial \phi_2(R_0, z, t)}{\partial r} = \frac{\partial R_0}{\partial t} + \frac{\partial R_0}{\partial z}\frac{\partial \phi_0(R_0, z, t)}{\partial z}, \tag{19}$$

$$0 = -\gamma_i + \frac{z}{Fr} - \left(\frac{\partial \phi_0(R_0, z, t)}{\partial z}\right)^2 - 2\frac{\partial \phi_0(R_0, z, t)}{\partial t}, \quad i = 1, 2. \tag{20}$$

The solution of (18) is

$$\phi_2(r, z) = -\frac{B''}{4}r^2 + C \ln r + D, \tag{21}$$

where the primes denote differentiation with respect to z, and C and D are functions of z and t.

Substitution of (21) into (19) yields

$$C = \frac{1}{2}\frac{\partial R_0^2}{\partial t} + \frac{1}{2}\frac{\partial (R_0^2 B')}{\partial z}, \tag{22}$$

Finally, the dynamic boundary conditions, i.e. (20), require that

$$-\gamma_i + \frac{z}{Fr} - \left(\frac{\partial B}{\partial z}\right)^2 - 2\frac{\partial B}{\partial t} = 0, \quad i = 1, 2. \tag{23}$$

Therefore, mathematical compatibility requires that $\gamma_1 = \gamma_2 = \gamma$, and

$$-\gamma + \frac{z}{Fr} - \left(\frac{\partial B}{\partial z}\right)^2 - 2\frac{\partial B}{\partial t} = 0, \tag{24}$$

which is analogous to the Bernoulli equation for one-dimensional, irrotational flows.

Equating terms of $O(\varepsilon^4)$ yields

$$\frac{\partial^2 \phi_2}{\partial z^2} + \frac{1}{r}\frac{\partial}{\partial r}\left(r\frac{\partial \phi_4}{\partial r}\right) = 0, \tag{25}$$

$$\frac{\partial \phi_4}{\partial r} + R_{i2}\frac{\partial^2 \phi_2}{\partial r^2} = \frac{\partial R_{i2}}{\partial t} + \frac{\partial R_0}{\partial z}\frac{\partial \phi_2}{\partial z} + \frac{\partial R_{i2}}{\partial z}\frac{\partial \phi_0}{\partial z}, \quad i = 1, 2, \tag{26}$$

$$\left(\frac{\partial \phi_2}{\partial r}\right)^2 = -2\frac{\partial \phi_0}{\partial z}\frac{\partial \phi_2}{\partial z} - 2\frac{\partial \phi_2}{\partial t}, \quad \text{at} \quad z = R_0. \tag{27}$$

The solution of (25) may be written as

$$\phi_4 = F + E \ln r - \frac{D''}{4}r^2 - \frac{C''}{4}r^2(\ln r - 1) + \frac{B''''}{64}r^4, \tag{28}$$

where E and F are functions of z and t.

Substraction of (26) and use of (22) imply that

$$\frac{\partial (b_2 R_0)}{\partial t} + \frac{\partial (b_2 R_0 B')}{\partial z} = 0, \tag{29}$$

which is a continuity equation.

Equation (27) may be expressed as

$$\left(-\frac{R_0}{2}B'' + \frac{C}{R_0}\right)^2 = -2B'\left(-\frac{R_0^2}{4}B'''' + C' \ln R_0 + D'\right) - 2\left(\frac{\partial D}{\partial t} + \frac{\partial C}{\partial t}\ln R_0 - \frac{R_0^2}{4}\frac{\partial B''}{\partial t}\right), \tag{30}$$

which is a partial differential equation for D.

The dynamic boundary conditions at the jet's interfaces to $O(\varepsilon^6)$ becomes

$$2\frac{\partial \phi_2}{\partial r}\left(\frac{\partial \phi_4}{\partial r} + R_{i2}\frac{\partial^2 \phi_2}{\partial r^2}\right) = -2\frac{\partial \phi_0}{\partial z}\left(\frac{\partial \phi_4}{\partial z} + R_{i2}\frac{\partial}{\partial z}\left(\frac{\partial \phi_2}{\partial r}\right)\right) - \left(\frac{\partial \phi_2}{\partial z}\right)^2 - 2\left(\frac{\partial \phi_4}{\partial t} + R_{i2}\frac{\partial}{\partial t}\left(\frac{\partial \phi_2}{\partial r}\right)\right), \quad i = 1, 2, \tag{31}$$

which may be subtracted to yield

$$\frac{R_0}{4}(B'')^2 - \frac{C^2}{R_0^3} = \frac{R_0}{2}B'B''' - \frac{B'C'}{R_0} + \frac{R_0}{2}\frac{\partial B''}{\partial t} - \frac{1}{R_0}\frac{\partial C}{\partial t}. \tag{32}$$

Equations (22), (24), (29) and (32) represent a system of partial differential equations for B', C, R_0 and b_2, and have the same form as those of the hydraulic model developed by Ramos[13] for thin, inviscid, incompressible, annular liquid jets; consequently, these equations may be solved by means of the adaptive finite difference method.[15] Once the values of B', C, R_0 and b_2 have been calculated, D may be determined from (30). Furthermore, (26) and (31) at $i = 1, 2$ yield four partial differential equations for E, F, R_{12} amd R_{22}.

The pressure can be expressed as

$$p = p_0 + \varepsilon^2 p_2 + O(\varepsilon^4), \tag{33}$$

which can be substituted together with (11) and the results obtained in this section into (10) to yield $p_0 = \gamma$, i.e. to leading order, the pressure is uniform throughout the jet and equal to the pressure of the gases which are enclosed by and surround the annular liquid jet.

2.2. $We = \infty$ and $Fr = O(\varepsilon^{-2})$

If there is no surface tension and $Fr = \varepsilon^{-2}F$ where $F = O(1)$, the regular perturbation expansion used in the previous section yields (16)–(26), (28) and (29) without the terms which contain the Froude number. For example, (24) becomes

$$-\gamma - \left(\frac{\partial B}{\partial z}\right)^2 - 2\frac{\partial B}{\partial t} = 0, \tag{34}$$

which indicates that, for steady jets, the axial velocity is uniform to leading order.

The dynamic boundary conditions to $O(\varepsilon^4)$ are

$$\left(\frac{\partial \phi_2(R_0, z, t)}{\partial r}\right)^2 = -2\frac{\partial \phi_0(R_0, z, t)}{\partial z}\frac{\partial \phi_2(R_0, z, t)}{\partial z} - 2\frac{\partial \phi_2(R_0, z, t)}{\partial t} + \frac{z}{F}, \tag{35}$$

which imply that

$$\left(-\tfrac{1}{2}B''R_0 + \frac{C}{R_0}\right)^2 = -2B'\left(-\tfrac{1}{4}B'''R_0^2 + C' \ln R_0 + D'\right) - 2\left(\frac{\partial D}{\partial t} + \frac{\partial C}{\partial t} \ln R_0 - \frac{R_0^2}{4}\frac{\partial B''}{\partial t}\right) + \frac{z}{F}, \tag{36}$$

which is a partial differential equation for D.

The dynamic boundary conditions to $O(\varepsilon^6)$ yield (31) and (32). Therefore, (22), (29), (32) and (34) represent a system of partial differential equations for B', C, R_0 and b_2. Once these values have been calculated, D may be determined from (36). The pressure at leading order coincides with that of the previous section.

It may be easily shown that $We = W\varepsilon^{-2}$, where $W = O(1)$, results in an inconsistency in the dynamic boundary conditions at the jet's interface at $O(\varepsilon^4)$.

2.3. $We = O(\varepsilon^{-4})$ and $Fr = (O(1)$

Surface tension effects can be easily included in the perturbation method employed in the previous section. If $We = O(1/\varepsilon^4)$, i.e. $We = W/\varepsilon^4$ and $W = O(1)$, equations (16)–(30) may be used, while the dynamic boundary conditions to $O(\varepsilon^6)$ become

$$2\frac{\partial \phi_2}{\partial r}\left(\frac{\partial \phi_4}{\partial r} + R_{12}\frac{\partial^2 \phi_2}{\partial r^2}\right) =$$

$$-2\frac{\partial \phi_0}{\partial z}\left(\frac{\partial \phi_4}{\partial z} + R_{12}\frac{\partial}{\partial z}\left(\frac{\partial \phi_2}{\partial r}\right)\right) - \left(\frac{\partial \phi_2}{\partial z}\right)^2 - 2\left(\frac{\partial \phi_4}{\partial t} + R_{12}\frac{\partial}{\partial t}\left(\frac{\partial \phi_2}{\partial r}\right)\right) + \frac{1}{WR_0}, \tag{37}$$

$$2\frac{\partial\phi_2}{\partial r}\left(\frac{\partial\phi_4}{\partial r}+R_{22}\frac{\partial^2\phi_2}{\partial r^2}\right)=$$

$$-2\frac{\partial\phi_0}{\partial z}\left(\frac{\partial\phi_4}{\partial z}+R_{22}\frac{\partial}{\partial z}\left(\frac{\partial\phi_2}{\partial r}\right)\right)-\left(\frac{\partial\phi_2}{\partial z}\right)^2-2\left(\frac{\partial\phi_4}{\partial t}+R_{22}\frac{\partial}{\partial t}\left(\frac{\partial\phi_2}{\partial r}\right)\right)-\frac{1}{WR_0}, \tag{38}$$

which may be subtracted to yield

$$\frac{R_0}{4}(B'')^2-\frac{C^2}{R_0^3}=\frac{R_0}{2}B'B'''-\frac{B'C'}{R_0}+\frac{R_0}{2}\frac{\partial B''}{\partial t}-\frac{1}{R_0}\frac{\partial C}{\partial t}-\frac{1}{WR_0b_2}. \tag{39}$$

Equations (22), (24), (29) and (39) represent a system of partial differential equations for B', C, R_0 and b_2. Once these values have been calculated, D may be determined from (30). The pressure at leading order coincides with that of Section 2.1, i.e. the liquid's pressure is identical to those of the gases enclosed by and surrounding the annular liquid jet. Note that (39) coincides with (32) for $W=\infty$.

2.4. $We=O(\varepsilon^{-4})$ and $Fr=O(\varepsilon^{-2})$

If $We=O(1/\varepsilon^4)$ and $Fr=O(1/\varepsilon^2)$, i.e. $We=W/\varepsilon^4$ and $Fr=F/\varepsilon^2$ with $W=O(1)$ and $F=O(1)$, it may be easily shown that (16)–(22), (25), (35), (37) and (38) hold. Therefore, B', C, R_0 and b_2 may be determined from (22), (29), (34) and (39), while D may be calculated from Eq. (36).

2.5. $We=O(\varepsilon^{-4})$ and $Fr=O(\varepsilon^{-4})$

If $We=O(1/\varepsilon^4)$ and $Fr=O(1/\varepsilon^4)$, i.e. $We=W/\varepsilon^4$ and $Fr=F/\varepsilon^4$ with $W=O(1)$ and $F=O(1)$, it may be easily shown that (16)–(22) and (25)–(30) hold, while the dynamic boundary conditions to $O(\varepsilon^6)$ become

$$2\frac{\partial\phi_2}{\partial r}\left(\frac{\partial\phi_4}{\partial r}+R_{12}\frac{\partial^2\phi_2}{\partial r^2}\right)=$$

$$-2\frac{\partial\phi_0}{\partial z}\left(\frac{\partial\phi_4}{\partial z}+R_{12}\frac{\partial}{\partial z}\left(\frac{\partial\phi_2}{\partial r}\right)\right)-\left(\frac{\partial\phi_2}{\partial z}\right)^2-2\left(\frac{\partial\phi_4}{\partial t}+R_{12}\frac{\partial}{\partial t}\left(\frac{\partial\phi_2}{\partial r}\right)\right)+\frac{z}{F}+\frac{1}{WR_0}, \tag{40}$$

$$2\frac{\partial\phi_2}{\partial r}\left(\frac{\partial\phi_4}{\partial r}+R_{22}\frac{\partial^2\phi_2}{\partial r^2}\right)=$$

$$-2\frac{\partial\phi_0}{\partial z}\left(\frac{\partial\phi_4}{\partial z}+R_{22}\frac{\partial}{\partial z}\left(\frac{\partial\phi_2}{\partial r}\right)\right)-\left(\frac{\partial\phi_2}{\partial z}\right)^2-2\left(\frac{\partial\phi_4}{\partial t}+R_{22}\frac{\partial}{\partial t}\left(\frac{\partial\phi_2}{\partial r}\right)\right)+\frac{z}{F}-\frac{1}{WR_0}, \tag{41}$$

which may be substracted to yield (39). Therefore, B', C, R_0 and b_2 may be determined from (22), (29), (34) and (39), while D may be calculated from (30).

The asymptotic analysis presented in Sections 2.1–2.5 results in a system of four partial differential equations for the leading order axial velocity component, mean radius, and thickness of the annular liquid jet (cf. (22), (24) and (29)) which are coupled to, for example, (32) which provides the value of C, i.e. the next to the leading term of the velocity potential (cf. (21)). Furthermore, the asymptotic analysis presented here is a long wavelength one which is not strictly applicable at the nozzle exit, even though boundary conditions at the nozzle exit will be used when solving (22), (24), (29) and (32) as

indicated in Section 4. Furthermore, it is important to indicate that the results of the five previous sections indicate that, if the Weber number is sufficiently large, mathematical compatibility requires that the pressure of the gases enclosed by the annular jet be identical to that of the gases surrounding the jet and identical to the liquid's pressure. Therefore, the results presented in Sections 2.1–2.5 are consistent with a hydraulic approximation to leading order in that the liquid's pressure is uniform throughout the jet. Furthermore (32) and (39) indicate that, in addition to $B(0, t)$, $R_0(0, t)$ and $b_2(0, t)$, an additional boundary condition must be provided. Such a boundary condition may be the specification of $\partial R_0(0, t)/\partial z$.

To handle a pressure difference between the gases enclosed by and surrounding the annular jet, surface tension effects must be much larger than those considered in the previous sections as indicated in the next section.

2.6. *We* = $O(1)$ *and* *Fr* = $O(1)$

If $We = O(1)$, and $Fr = O(1)$, equations (11)–(13) may be used to obtain (16)–(19), while the terms $1/WeR_0$ and $-1/WeR_0$ must be added to the right hand sides of (20) for $i = 1$ and 2, respectively, i.e. (20) becomes

$$-\gamma_1 + \frac{z}{Fr} - \left(\frac{\partial B}{\partial z}\right)^2 - 2\frac{\partial B}{\partial t} + \frac{1}{WeR_0} = 0, \tag{42}$$

$$-\gamma_2 + \frac{z}{Fr} - \left(\frac{\partial B}{\partial z}\right)^2 - 2\frac{\partial B}{\partial t} - \frac{1}{WeR_0} = 0. \tag{43}$$

Equations (42) and (43) can be substracted and added to yield, respectively,

$$\gamma_1 - \gamma_2 = \frac{2}{WeR_0}, \tag{44}$$

$$-\frac{\gamma_1 + \gamma_2}{2} + \frac{z}{Fr} - (B')^2 - 2\frac{\partial B}{\partial t} = 0. \tag{45}$$

Equation (44) indicates that the difference between the pressure of the gases enclosed by and those surrounding the annular liquid jet is balanced by surface tension effects, whereas (45) shows that surface tension does not affect the leading order axial velocity component.

Equations (22), (29), (44) and (45) may be solved to obtain the values of B', C, R_0 and b_2. Furthermore, it must be indicated that, for $We = O(1)$, closure of the equations at leading order is achieved without invoking the dynamic boundary conditions at $O(\varepsilon^6)$, while the analysis presented in Sections 2.1–2.5 required these boundary conditions.

2.7. *We* = $O(1)$ *and* *Fr* = $O(\varepsilon^{-2})$

If $We = O(1)$ and $Fr = F\varepsilon^{-2}$ where $F = O(1)$, it may be easily shown that the equations governing the flow are (22), (29), (44) and

$$-\frac{\gamma_1 + \gamma_2}{2} - (B')^2 - 2\frac{\partial B}{\partial t} = 0. \tag{46}$$

Equation (46) indicates that gravity does not affect the liquid's axial velocity component at leading order, and (22), (29), (44) and (46) may be solved to obtain the values of B', C, R_0 and b_2.

Since a large surface tension implies that the Weber number is small and since the Weber number is the square of the ratio of a characteristic axial velocity at the nozzle exit, u_0^*, to the capillary velocity,

$u_c^* = (\sigma^*/\rho^* R_0^*)^{1/2}$, a small Weber number implies that the capillary velocity is larger than that at the nozzle exit. Therefore, asymptotic analyses of large surface tension, i.e., capillary, annular jets may be conveniently performed by nondimensionalizing the liquid's axial velocity with respect to the capillary velocity as indicated in the next section.

3. ASYMPTOTIC ANALYSIS OF CAPILLARY, ANNULAR LIQUID JETS

If the axial and radial co-ordinates, velocity potential, annular jet's radii and pressure with respect to $L^*, R_0^*, u_c^* L^*, R_0^*$ and $\rho^* u_c^{*2}/2$, respectively, so that (1)–(5) become (6), (7), and

$$\left(\frac{\partial\phi(R_1,z,t)}{\partial r}\right)^2 = \varepsilon^2\left(-\gamma_1 - \left(\frac{\partial\phi(R_1,z,t)}{\partial z}\right)^2 - 2\frac{\partial\phi(R_1,z,t)}{\partial t} + \frac{zBo}{\varepsilon} + \frac{1}{R_1(1+\varepsilon^2(\partial R_1/\partial z)^2)^{1/2}} - \frac{\varepsilon^2(\partial^2 R_1/\partial z^2)}{(1+\varepsilon^2(\partial R_1/\partial z)^2)^{3/2}}\right), \tag{47}$$

$$\left(\frac{\partial\phi(R_2,z,t)}{\partial r}\right)^2 = \varepsilon^2\left(-\gamma_2 - \left(\frac{\partial\phi(R_2,z,t)}{\partial z}\right)^2 - 2\frac{\partial\phi(R_2,z,t)}{\partial t} + \frac{zBo}{\varepsilon} - \frac{1}{R_2(1+\varepsilon^2(\partial R^2/\partial z)^2)^{1/2}} + \frac{\varepsilon^2(\partial^2 R_2/\partial z^2)}{(1+\varepsilon^2(\partial R_2/\partial z)^2)^{3/2}}\right), \tag{48}$$

$$p = -\left(2\frac{\partial\phi}{\partial t} + \frac{1}{\varepsilon^2}\left(\frac{\partial\phi}{\partial r}\right)^2 + \left(\frac{\partial\phi}{\partial z}\right)^2\right) + \frac{zBo}{\varepsilon}, \tag{49}$$

where $Bo = 2\rho^* g^* R_0^{*2}/\sigma^*$ is the Bond number.

If $Bo = \hat{B}\varepsilon$, where $\hat{B} = O(1)$, substitution of (11)–(13) into (6), (7), (47) and (48) and expansion of the interface boundary conditions in Taylor's series yield (22) and (29), while (47) and (48) become to $O(\varepsilon^2)$

$$-\gamma_1 + z\hat{B} - \left(\frac{\partial B}{\partial z}\right)^2 - 2\frac{\partial B}{\partial t} + \frac{1}{R_0} = 0, \tag{50}$$

$$-\gamma_2 + z\hat{B} - \left(\frac{\partial B}{\partial z}\right)^2 - 2\frac{\partial B}{\partial t} - \frac{1}{R_0} = 0. \tag{51}$$

Equations (50) and (51) can be substracted and added to yield, respectively,

$$\gamma_1 - \gamma_2 = \frac{2}{R_0}, \tag{52}$$

$$-\frac{\gamma_1+\gamma_2}{2} + z\hat{B} - (B')^2 - 2\frac{\partial B}{\partial t} = 0. \tag{53}$$

Equation (52) indicates that the difference between the pressure of the gases enclosed by and those surrounding the annular liquid jet is balanced by surface tension effects, whereas (53) shows that surface tension does not affect the leading order axial velocity component. Equations (22), (29), (52) and (53) may be solved to obtain the values of B', C, R_0 and b_2.

If $Bo = \hat{B}\varepsilon^3$, where $\hat{B} = O(1)$, equation (53) is to be replaced by

$$-\frac{\gamma_1 + \gamma_2}{2} - (B')^2 - 2\frac{\partial B}{\partial t} = 0, \tag{54}$$

which together with (22), (29) and (52) may be solved to obtain the values of B', C, R_0 and b_2.

4. STEADY, ANNULAR LIQUID JETS

The one-dimensional models of thin, slender, annular liquid jets presented in Sections 2.1–2.5 may be compactly written as (cf. (22), (24), (29) and (32))

$$\frac{\partial(b_2 R_0)}{\partial t} + \frac{\partial(b_2 R_0 U)}{\partial z} = 0, \tag{55}$$

$$\frac{\partial U}{\partial t} + U\frac{\partial U}{\partial z} = \frac{1}{2G}, \tag{56}$$

$$\frac{1}{2}\frac{\partial R_0^2}{\partial t} + \frac{1}{2}\frac{\partial(R_0^2 U)}{\partial z} = C, \tag{57}$$

$$\frac{\partial C}{\partial t} + U\frac{\partial C}{\partial z} = \left(\frac{C}{R_0}\right)^2 - \frac{1}{Hb_2} - \frac{3R_0^2}{4}\left(\frac{\partial U}{\partial z}\right)^2, \tag{58}$$

where $U = B'$, and $(G, H) = (Fr, \infty)$, (∞, ∞), (Fr, W), (∞, ∞), and (∞, ∞) for the flow regimes analysed in Sections 2.1–2.5 respectively.

The capillary flow regimes presented in Sections 2.6 and 2.7 are governed by (55), (56), and

$$R_0 = \frac{2}{We(\gamma_1 - \gamma_2)}, \tag{59}$$

while those of Section 4 are governed by (55),

$$\frac{\partial U}{\partial t} + U\frac{\partial U}{\partial z} = \frac{1}{2M}, \tag{60}$$

and

$$R_0 = \frac{2}{\gamma_1 - \gamma_2}, \tag{61}$$

where $M = \hat{B}$ and ∞ for $Bo = \varepsilon\hat{B}$ and $Bo = \varepsilon^3\hat{B}$ respectively (cf. (53) and (54)).

For steady annular liquid jets, the leading order (55)–(58), and (55), (56) and (59) have analytical solutions which are described in the next paragraphs.

4.1. Inertia-dominated jets

The steady state solutions of (55) and (56) can be written as

$$UR_0 b_2 = \beta, \quad U = (1 + z/G)^{1/2}, \tag{62a, b}$$

where β denotes the (constant) volumetric flow rate and may be set to one without loss of generality, and the leading order axial velocity has been assumed to be valid up to the nozzle exit (cf. (60)). Equation (62b) is Torricelli's free-fall law.

For steady jets, (57) and (58) may be written as

$$\psi' = C, \tag{63}$$

$$\psi'' = \frac{2\psi^2 UU'' + (CU)^2 - (\psi U')^2 - (2\psi U)^{3/2}/H\beta}{2\psi U^2}. \tag{64}$$

$$R_0 = (2\psi/U)^{1/2}, \tag{65}$$

where

$$\psi = \tfrac{1}{2} UR_0^2, \tag{66}$$

and

$$b_2 = \beta/UR_0. \tag{67}$$

Equations (63)–(67) may be solved numerically by means of, for example, a fourth-order accurate Runge–Kutta method, to obtain the values of ψ and R_0, and (62a) may be used to determine b_2. Equations (63) and (64) demand that the values of, for example, R_0, b_2 and dR_0/dz be specified at the nozzle exit, i.e., at $z = 0$.

4.2. Surface tension-dominated jets

The steady state fluid dynamics of surface tension-dominated annular jets are governed by (59) and (62) if the variables are non-dimensionalized as in Section 2, or by

$$UR_0 b_2 = \beta, \quad U = (1 + z/M)^{1/2}, \tag{68}$$

and

$$R_0 = \frac{2}{\gamma_1 - \gamma_2}, \tag{69}$$

if the non-dimensionalization of Section 3 is employed. Note that the leading order axial velocity component has been assumed to be valid up to the nozzle exit.

Since, according to (69), the mean radius of the annular jet is constant, surface-dominated jets will not be considered further in this paper. Note that even for unsteady jets, the capillary regime is characterized by a jet's mean radius which is, at most, a function of time (cf. (59)).

5. COMPARISON WITH OTHER MODELS

For large Weber numbers, the steady state solutions of the asymptotic equations presented in the previous section indicate that the axial velocity component of the liquid at leading order is governed by Torricelli's free-fall law (cf. (62b)). The same law was found to govern the steady fluid dynamics of the one-dimensional, hydraulic model of annular liquid jets developed by Ramos[13] if the jet's convergence length is much larger than the jet's mean radius at the nozzle exit. For this reason and in order to understand the advantages and limitations of the one-dimensional models of annular liquid jets developed in this paper, it is convenient to compare their formulations with that of Reference 13.

Using the same non-dimensionalization as in Section 2 for z, R and t, the hydraulic model of Reference 13 may be written as

$$\frac{\partial(Rb)}{\partial t}+\frac{\partial(uRb)}{\partial z}=0, \tag{70}$$

$$\frac{\partial}{\partial t}(uRb)+\frac{\partial}{\partial z}\left(u^2Rb\right)=\pm\frac{Rb}{2Fr}+\left(\frac{\gamma_2-\gamma_1}{2}+\frac{J}{We}\right)R\frac{\partial R}{\partial z}, \tag{71}$$

$$\frac{\partial}{\partial t}(vRb)+\frac{\partial}{\partial z}(uvRb)=-\left(\frac{\gamma_2-\gamma_1}{2}+\frac{J}{We}\right)\frac{R}{\varepsilon^2}, \tag{72}$$

$$v=\frac{\partial R}{\partial t}+u\frac{\partial R}{\partial z}. \tag{73}$$

$$J=\frac{1}{R(1+(\varepsilon\partial R/\partial z)^2)^{1/2}}-\varepsilon^2\frac{\partial^2R/\partial z^2}{(1+(\varepsilon\partial R/\partial z)^2)^{3/2}}, \tag{74}$$

where $u=u^*/u_0^*, v=v^*/\varepsilon u_0^*, R=R^*/R_0^*$ and $b=b^*/R_0^*$ denote the average axial and radial velocity components, and the jet's mean radius and thickness, respectively, and the asterisk denotes dimensional quantities.

Equations (55)–(58) or (55), (59) and (60) have the same form and are of the same type as (70)–(73); therefore, they may be solved by means of the adaptive finite difference method developed in Reference 15 which maps the time-dependent, curvilinear geometry of the annular liquid jet into a unit square, employs upwind differences for the convection terms, and uses an iterative, block bidiagonal technique to determine the values of the dependent variables at each grid point. Despite the similarities between (55)–(58) and (70)–(73), there are substantial differences between them. First, (70)–(73) were obtained by integrating the Euler equations along the jet's thickness, applying the kinematic and dynamic boundary conditions at the jet's interfaces, using Taylor's series expansions around the jet's mean radius, and assuming that the jet's axial and radial velocity components are not functions of the radial co-ordinate.[13] On the other hand, (55)–(58) have been derived by means of asymptotic expansions in Section 2.

Second, the hydraulic model represented by (70)–(73) allows for a pressure difference between the gases enclosed by and surrounding the annular jet, whereas the models developed in Sections 2.1–2.5 imply that $\gamma_1=\gamma_2$. Third, if the dependent variables in (70)–(73) are expanded as

$$u=u_0+\varepsilon^2u_2+O(\varepsilon^4), \quad v=v_0+\varepsilon^2v_2+O(\varepsilon^4), \tag{75}$$

$$R=R_0+\varepsilon^2R_2+O(\varepsilon^4), \quad b=\varepsilon^2b_2+O(\varepsilon^4), \tag{76}$$

$We=O(1)$ and $\gamma_1-\gamma_2=O(1)$, equation (72) is, at leading order, i.e. $O(\varepsilon^0)$, identical to (59), while (70) and (71) are identical to (55) and (56) to leading order. Equation (73) is, at $O(\varepsilon^0)$,

$$v_0=\frac{\partial R_0}{\partial t}+u_0\frac{\partial R_0}{\partial z}, \tag{77}$$

where the second term in the right-hand side of this equation is zero since, according to (59), R_0 is only a function of time.

The same results may be obtained if $We=W/\varepsilon^2$ and $\gamma_1-\gamma_2=\varepsilon^2(\hat{\gamma}_1-\hat{\gamma}_2)$, where W and $(\hat{\gamma}_1-\hat{\gamma}_2)$ are $O(1)$. Furthermore, if $\gamma_1=\gamma_2$ and $We=\infty$ or $We=\mathrm{W}/\varepsilon^4$, where $W=O(1)$, it may be easily

shown that, to leading order, (70) and (71) are identical to (55) and (56), respectively, (73) is identical to (77), and (72) becomes

$$\frac{\partial v_0}{\partial t} + u_0 \frac{\partial v_0}{\partial z} = \frac{1}{ZR_0 b_2} \frac{\partial R_0}{\partial z}, \tag{78}$$

where $Z = \infty$ or $Z = W$ if $We = \infty$ or W/ε^4 respectively. Furthermore, (77) and (78) may be combined to obtain (57) and (58). Therefore, the hydraulic model of Reference 13 includes the one-dimensional models presented in this paper, and its formulation accounts for a pressure difference between the gases enclosed by and surrounding the annular liquid jet. Since the axial and radial velocity components of the liquid were assumed to be independent of the radial coordinate, the hydraulic model is only valid for thin annular jets.

Equations (70)–(73) may also be used to study the fluid dynamics of annular liquid membranes, i.e. annular jets of zero thickness, by simply replacing Rb by m, where m denotes the annular membrane's mass per unit length and per radian.

6. PRESENTATION OF RESULTS

The one-dimensional models presented in Sections 4 have been used to determine the fluid dynamics of steady, upward and downward annular liquid jets as indicated Sections 6.1 and 6.2, respectively, by solving (63)–(67) by means of a fourth-order accurate Runge–Kutta method with $\Delta z = 0{\cdot}001$. Equations (55)–(58) were solved by means of the adaptive finite difference method presented in Reference 15 in order to determine the shape and velocity field of steady, upward and downward annular liquid jets. The largest differences between the results of the Runge–Kutta and adaptive finite difference methods were of the order of 10^{-3}.

The hydraulic model discussed in Section 5 accounts for pressure differences between the gases enclosed by and surrounding the annular jet, and was used to study the effects of gravitational modulation on the unsteady fluid dynamics of annular liquid jets as indicated in Section 6.3.

6.1. Steady, upward, annular liquid jets

Some sample results illustrating the shape of steady, upward, annular liquid jets are presented in Figures 2–6. Figures 2–4 correspond $R_0(0) = b_2(0) = 1$, $\varepsilon = 0.1$, $Fr = -1$, and $dR_0(0)/dz = -0{\cdot}25$, 0 and 0·25, respectively, and several Weber numbers. Figure 2 corresponds to inwardly directed flows at the nozzle exit, i.e. flows directed toward the symmetry axis, and shows the thickening of the annular liquid downstream of the nozzle; this thickening is due to the gravitational acceleration which opposes the jet's motion. Figure 2 also shows that the jet's thickness reaches large values near $z = 1$. This result is consistent with (62) which indicates that the leading order axial velocity component becomes zero at $z = -G$, for $G < 0$; at this location, the jet's thickness becomes infinite according to (62a). Figure 2 also indicates that the axial location at which the axial velocity becomes zero increases as the Weber number is increased.

Figures 3 and 4 correspond to axial and outwardly directed, respectively, flows at the nozzle exit, and exhibit similar trends to those of Figure 2. These three figures also indicate that the jet's shape is not very sensitive to the Weber number for $We \geqslant 100$.

Figure 5 corresponds $R_0(0) = b_2(0) = 1$, $\varepsilon = 0{\cdot}1$, $We = 100$, $dR_0(0)/dz = 0$, and two different values of the Froude number, and indicates that the axial location at which the axial velocity component of the annular liquid jet becomes zero increases as the Froude number is increased. This result is again consistent with (62b) which indicates that the leading order axial velocity component becomes zero at $z = -G$, for $G < 0$.

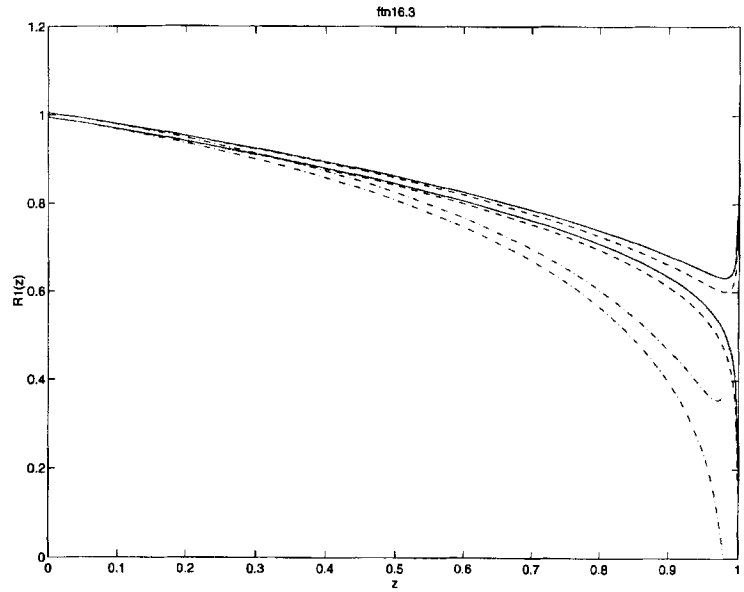

Figure 2. Steady, upward, annular liquid jets ($Fr = -1$, $R_0(0) = b_2(0) = 1$, $dR(0)/dz = -0{\cdot}25$, $\varepsilon = 0{\cdot}1$, and $We = \infty$ (solid lines), 100 (dashed lines), 10 (dashed-dotted lines))

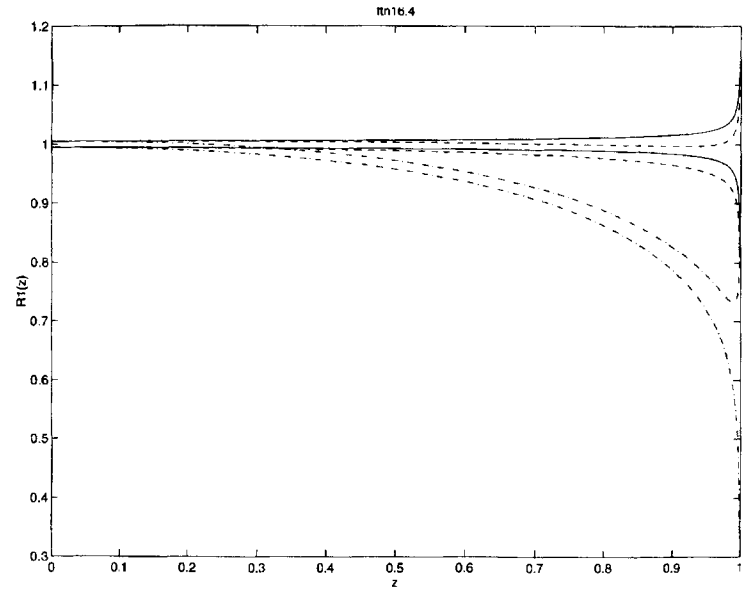

Figure 3. Steady, upward, annular liquid jets ($Fr = -1$, $R_0(0) = b_2(0) = 1$, $dR(0)/dz = 0$, $\varepsilon = 0{\cdot}1$, and $We = \infty$ (solid lines), 100 (dashed lines), 10 (dashed-dotted lines))

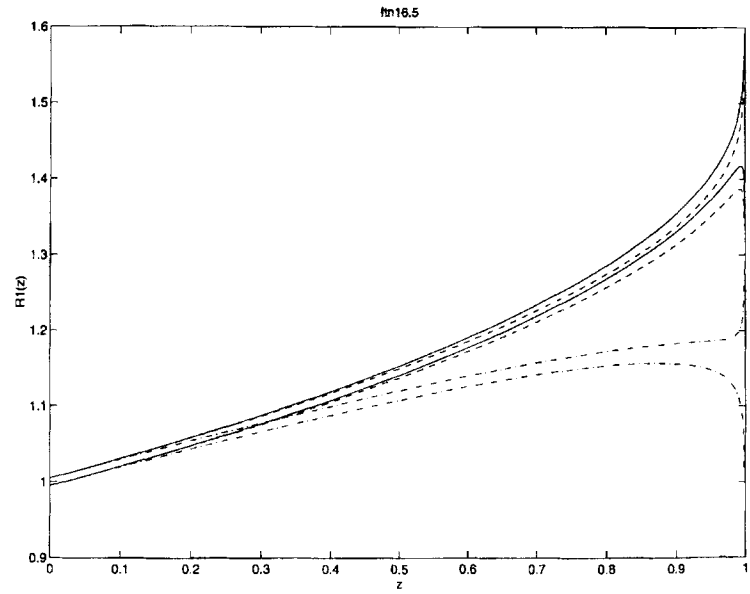

Figure 4. Steady, upward, annular liquid jets ($Fr = -1$, $R_0(0) = b_2(0) = 1$, $dR(0)/dz = 0{\cdot}25$, $\varepsilon = 0{\cdot}1$, and $We = \infty$ (solid lines), 100 (dashed lines), 10 (dashed-dotted lines))

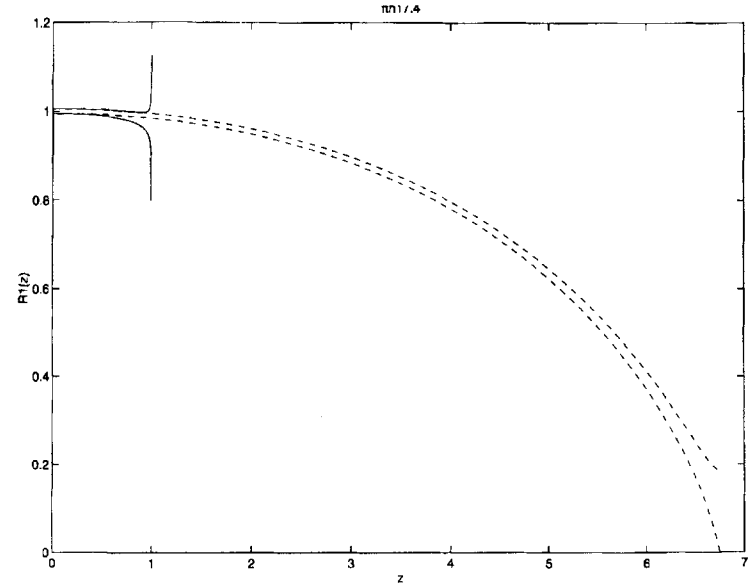

Figure 5. Steady, upward, annular liquid jets ($We = 100$, $R_0(0) = b_2(0) = 1$, $dR(0)/dz = 0$, $\varepsilon = 0{\cdot}1$, and $Fr = -1$ (solid lines), -10 (dashed lines)

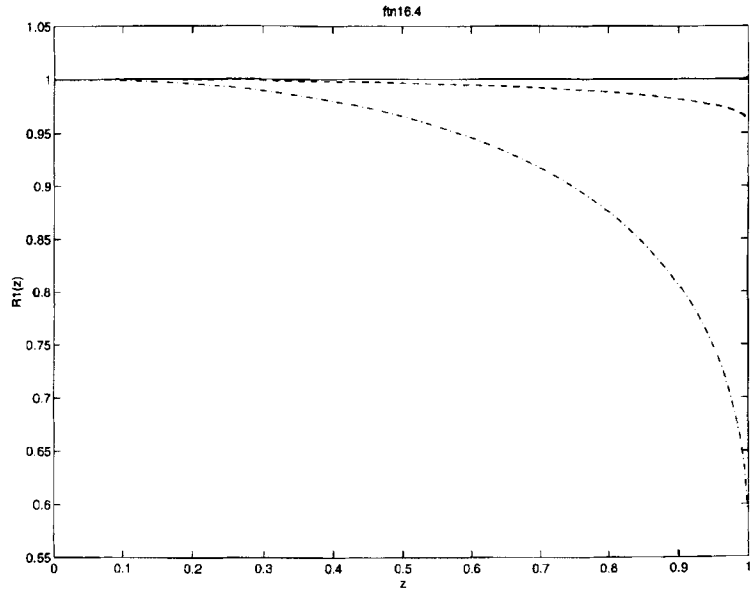

Figure 6. Steady, upward, annular liquid jets ($Fr = -1$, $R_0(0) = b_2(0) = 1$, $dR(0)/dz = 0$, $\varepsilon = 0{\cdot}01$, and $We = \infty$ (solid lines), 100 (dashed lines), 10 (dashed-dotted lines))

Figure 6 corresponds $R_0(0) = b_2(0) = 1$, $\varepsilon = 0{\cdot}01$, $Fr = -1$, and $dR_0(0)/dz = 0$ respectively, and several Weber numbers, i.e. it corresponds to thinner annular liquid jets than those shown in Figure 3. Figures 3 and 6 indicate that the axial location at which the axial velocity component of upward jets tends to zero at the theoretical limit of $z = -G$ increases as the thickness of the jet at the nozzle exit is decreased.

6.2. Steady, downward, annular liquid jets

Some sample results illustrating the shape of steady, downward, annular liquid jets are presented in Figures 7–11. Figures 7–9 correspond $R_0(0) = b_2(0) = 1$, $\varepsilon = 0{\cdot}1$, $Fr = 1$, and $dR_0(0)/dz = -0{\cdot}25$, 0 and 0·25, respectively, and several Weber numbers. Figure 7 corresponds to inwardly directed flows at the nozzle exit, i.e. flow directed toward the symmetry axis, and shows the thicknening of the annular liquid at the convergence point, i.e. at the axial location where the jet's inner radius becomes zero. Figure 7 also indicates that the convergence length increases as the Weber number is increased; therefore, the validity of the slender approximation used in this paper increases as the Weber number is increased.

Figures 8 and 9 correspond to axial and outwardly directed, respectively, flows at the nozzle exit, and exhibit similar trends to those of Figure 7, i.e. the convergence length increases as the Weber number is increased. Although not shown here, the convergence length for axially directed flows at the nozzle exit and $We = 100$ is about 30, while no convergence was observed for $z \leqslant 100$ for $We = \infty$. The same holds for $We = 100$ and ∞ in Figure 9. Figures 7–9 also indicate that the jet's convergence length increases as the slope of the annular liquid jet at the nozzle exit is increased.

Figure 10 corresponds $R_0(0) = b_2(0) = 1$, $\varepsilon = 0{\cdot}1$, $We = 100$, $dR_0(0)/dz = 0$, and two different values of the Froude number, and indicates that the convergence length increases as the Froude umber is decreased, i.e. as the gravitational acceleration is increased with respect to the flow inertia at the nozzle exit.

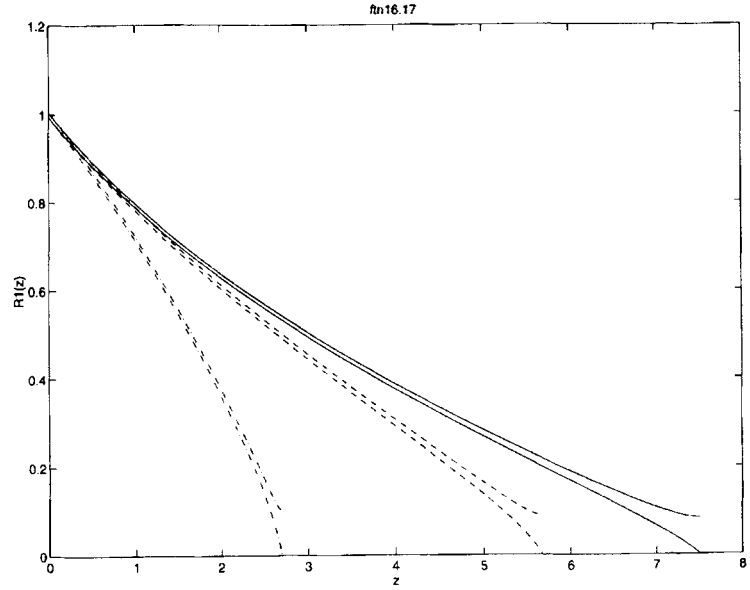

Figure 7. Steady, downward, annular liquid jets ($Fr = 1$, $R0(0) = b_2(0) = 1$, $dR(0)/dz = -0{\cdot}25$, $\varepsilon = 0{\cdot}1$, and $We = \infty$ (solid lines), 100 (dashed lines), 10 (dashed-dotted lines))

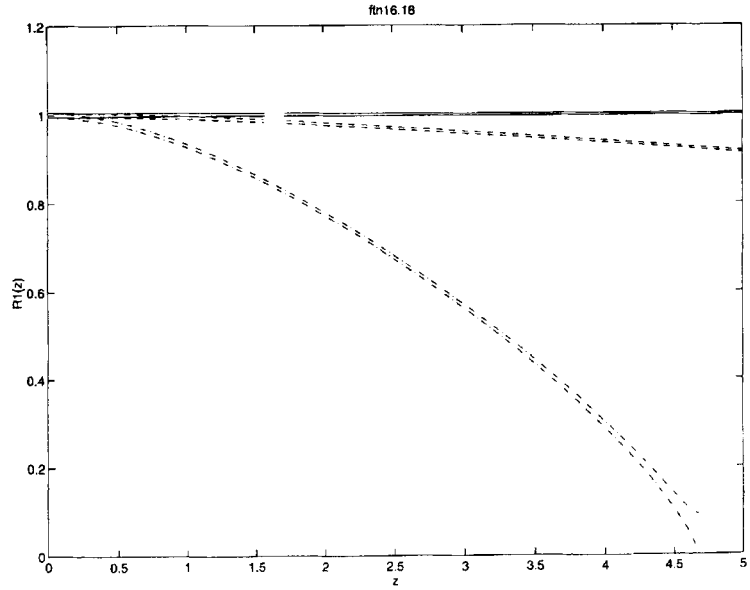

Figure 8. Steady, downward, annular liquid jets ($Fr = 1$, $R_0(0) = b_2(0) = 1$, $dR(0)/dz = 0$, $\varepsilon = 0{\cdot}1$, and $We = \infty$ (solid lines), 100 (dashed lines), 10 (dashed-dotted lines))

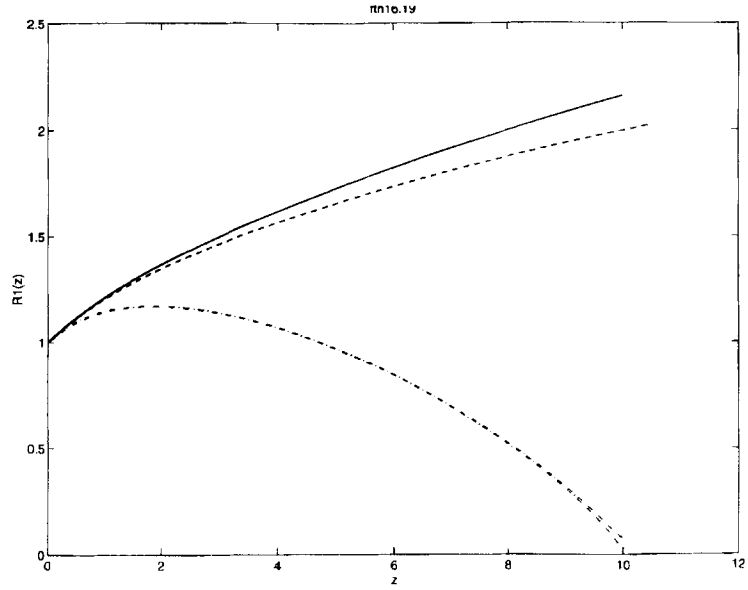

Figure 9. Steady, downward, annular liquid jets ($Fr = 1$, $R_0(0) = b_2(0) = 1$, $dR(0)/dz = 0{\cdot}25$, $\varepsilon = 0{\cdot}1$, and $We = \infty$ (solid lines), 100 (dashed lines), 10 (dashed-dotted lines))

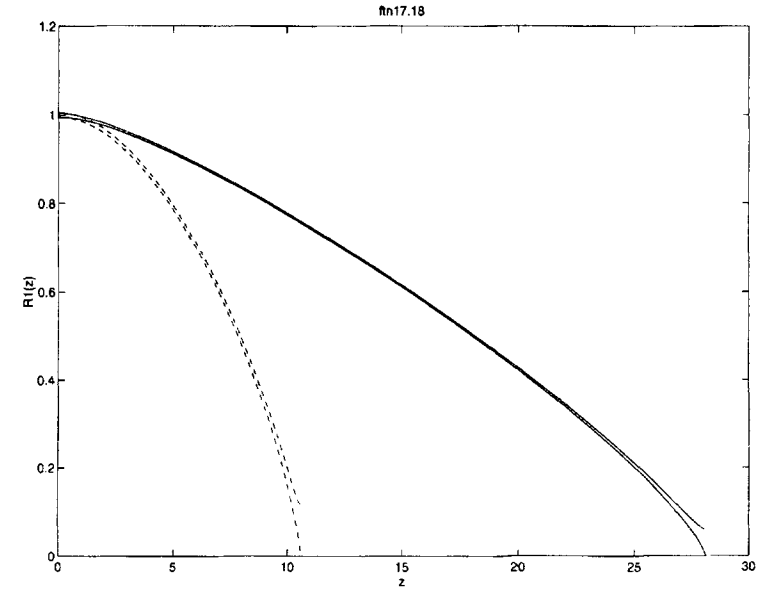

Figure 10. Steady, downward, annular liquid jets ($We = 100$, $R_0(0) = b_2(0) = 1$, $dR(0)/dz = 0$, $\varepsilon = 0{\cdot}1$, and $Fr = 1$ (solid lines), 10 (dashed lines))

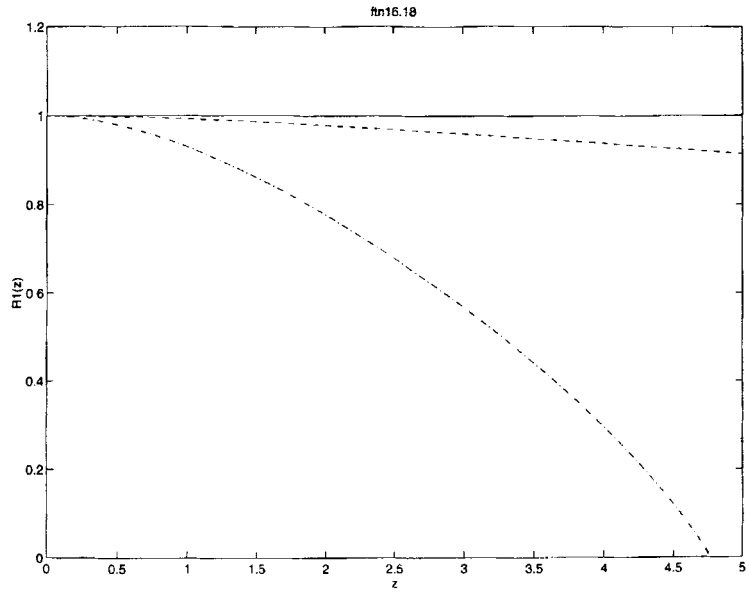

Figure 11. Steady, downward, annular liquid jets ($Fr = 1$, $R_0(0) = b_2(0) = 1$, $dR(0)/dz = 0$, $\varepsilon = 0{\cdot}01$, and $We = \infty$ (solid lines), 100 (dashed lines), 10 (dashed-dotted lines))

Figure 11 corresponds $R_0(0) = b_2(0) = 1$, $\varepsilon = 0{\cdot}01$, $Fr = 1$, and $dR_0(0)/dz = 0$ respectively, and several Weber numbers, i.e. it corresponds to thinner annular liquid jets than those shown in Figure 8. Figures 8 and 11 indicate that the convergence length increases slightly as the annular jet's thickness at the nozzle exit is increased.

6.3. *Annular liquid jets subject to gravity modulation*

The hydraulic model reviewed in Section 5 may be used to determine the effects of time-dependent boundary conditions at the nozzle exit, unsteady gas injection into the volume enclosed by the jet, and fluctuating body forces on the unsteady dynamics of annular liquid jets. In this section, the effects of gravity modulation on isothermal, downward, annular liquid jets are considered in the absence of mass injection into the volume enclosed by and mass absorption by the annular jet. These effects are analogous to those that occur when the annular jet is translated with an axial acceleration parallel to the z-axis without rotation. In this case, the velocity components that appear in the hydraulic model of Section 5 are relative to the non-inertial frame of reference.

Instead of using the nondimensionalization of Section 2, the equations of the hydraulic model may be written as

$$\frac{\partial m}{\partial t} + \frac{\partial (mu)}{\partial z} = 0, \tag{79}$$

$$\frac{\partial}{\partial t}(mu) + \frac{\partial}{\partial z}(mu^2) = mQ + \frac{1}{We}(-C_{pn} + J)R\frac{\partial R}{\partial z}, \tag{80}$$

$$\frac{\partial}{\partial t}(mv) + \frac{\partial}{\partial z}(muv) = \frac{1}{We}(C_{pn} - J)R, \tag{81}$$

$$v = \frac{\partial R}{\partial t} + u\frac{\partial R}{\partial z}. \tag{82}$$

$$J = \frac{1}{R(1+(\partial R/\partial z)^2)^{1/2}} - \frac{\partial^2 R/\partial z^2}{(1+(\partial R/\partial z)^2)^{3/2}}, \tag{83}$$

where lengths, time and velocity components have been nondimensionalized with respect to $R_0^*, R_0^*/u_0^*$ and u_0^*, respectively, $Q = g^* R_0^*/u_0^{*2}$ is the inverse of the Froude number, $We = m_0^* u_0^{*2}/2\sigma^* R_0^*$, $m = Rb$, $m_0^* = \rho^* R_0^* b_0^*$ and

$$C_{pn} = C_{p\max}\left(\frac{p_1^*}{p_2^*} - 1\right), \quad C_{p\max} = \frac{p_2^* R_0^*}{2\sigma^*}. \tag{84}$$

Equations (79)–(83) have been solved subject to the following boundary conditions at the nozzle exit

$$m(0,t) = b_0^*/R_0^*, \quad R(0,t) = v(0,t) = 1, \quad v(0,t) = 0, \tag{85}$$

and a gravitational acceleration which is a periodic function of time. For a sinusoidal gravitational modulation, i.e.

$$g^* = g_0^*(1 + a\sin(\omega^* t^*)) \tag{86}$$

where g_0^*, a and ω^* are a (constant) mean gravitational acceleration, the non-dimensional amplitude and the dimensional frequency of the gravitational fluctuations respectively. For experiments carried out aboard spacecraft, the intermittent sinusoidal gravitational acceleration of (86) may correspond to intermittent firings of rockets for attitude control, crew motions, etc.

Using the non-dimensionalizations described above, the inverse of the Froude number may be written as

$$Q = \frac{1}{Fr} = \frac{1}{Fr_0}(1 + a\sin(2\pi St)), \tag{87}$$

where $Fr_0 = g_0^* R_0^*/u_0^{*2}$, and $S = \omega^* R_0^*/2\pi u_0^*$ is the Strouhal number.

Since gravitational fluctuations produce changes in the shape of the annular liquid jet, one must account for the compression and expansion of the gases enclosed by and surrounding the annular liquid jet. Here, the gases surrounding the annular liquid jet have been assumed to be infinite in extent and $p_2^* =$ const., while those enclosed by the jet have been assumed to be isothermal so that

$$\frac{p_1^*(t)}{p_2^*}\int_0^{L(t)} R_1(z,t)\mathrm{d}z = \frac{p_1^*(0)}{p_2^*}\int_0^{L(0)} R_1(z,0)\mathrm{d}z = \text{const.}, \tag{88}$$

where L denotes the convergence length, i.e. $R_1(L(t), t) = 0$.

Equations (79)–(83) were solved by means of the adaptive finite difference method of Reference 15 with $a = 0$ until a steady state solution of these equations was found. Once a steady state was reached, the time was set to zero and the gravitational modulation was applied. Calculations were performed until all the flow variables were periodic functions of time. Some sample results corresponding to $p_1^*(0) = p_2^*, We = 50, Fr_0 = 10$, and $b_0^*/R_0^* = 0{\cdot}05$ are illustrated in Figures 12–14 for periodic, rectangular, gravitational modulations with $S = 0{\cdot}1$ and $a = 0{\cdot}25$, $0{\cdot}75$ and $1{\cdot}50$ respectively. These figures indicate that the pressure coefficient and the convergence length (which has been normalized with respect to that at steady state) are periodic functions of time which have the same frequency as that of the gravitational modulation; their amplitudes increase as a is increased. The phase diagram for the convergence length has been drawn for

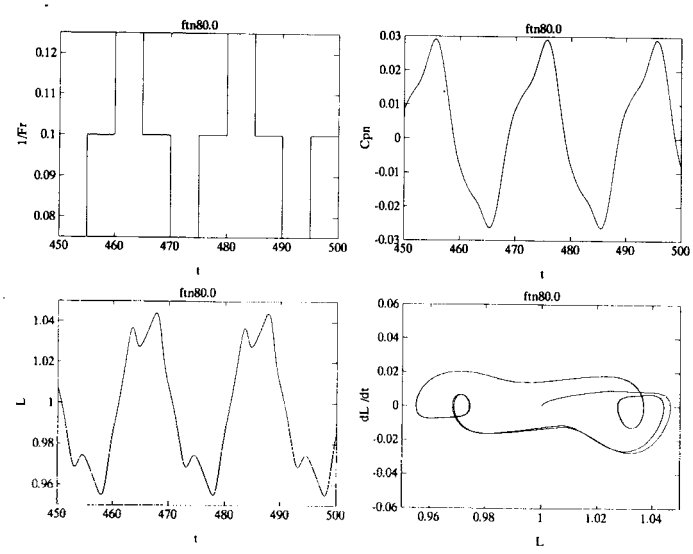

Figure 12. Inverse of the Froude number (top left), pressure coefficient (top right), convergence length (bottom left) and phase diagram for the convergence length (bottom right) as functions of time ($a = 0{\cdot}25$, $S = 0{\cdot}1$, pulse width = time between pulses = 5)

$t \geqslant 0$ in order to illustrate the dynamics of the convergence length from the initial steady state (with $a = 0$) until a periodic solution is reached, and undergoes large changes as a is increased.

Figures 15–17 also correspond to a rectangular, gravitational modulation of $a = 0{\cdot}25$ and $S = 0{\cdot}1$, and illustrate the effects of the separation or time between rectangular pulses on the dynamic response of the annular liquid jet. For a purely rectangular modulation, Figure 15 indicates that the pressure coefficient and convergence length are periodic functions of time and have small amplitudes. The amplitude of these oscillations and the distortion of the phase diagram for the

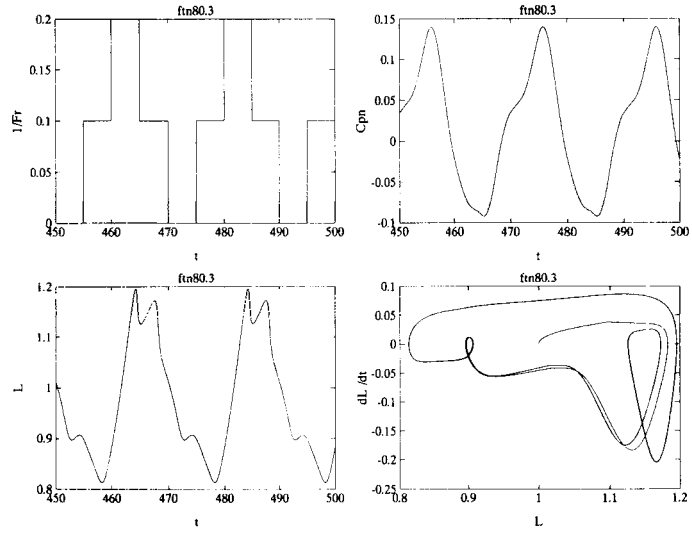

Figure 13. Inverse of the Froude number (top left), pressure coefficient (top right), convergence length (bottom left) and phase diagram for the convergence length (bottom right) as functions of time ($a = 0{\cdot}75$, $S = 0{\cdot}1$, pulse width = time between pulses = 5)

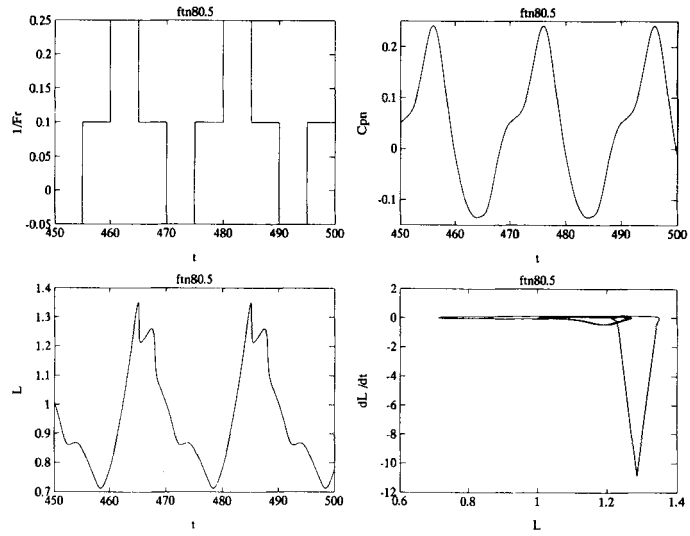

Figure 14. Inverse of the Froude number (top left), pressure coefficient (top right), convergence length (bottom left) and phase diagram for the convergence length (bottom right) as functions of time ($a = 1{\cdot}50$, $S = 0{\cdot}1$, pulse width = time between pulses = 5)

convergence length increase as the separation between rectangular pulses is increased (cf. Figure 16). Further increases in the separation between pulses result in a decrease of the amplitude of both the convergence length and the pressure coefficient and in the formation of two loops in the phase diagram for the convergence length as shown in Figure 18. Note that, in the absence of gravitational modulation, the values of the pressure coefficient and non-dimensionalized convergence length are zero and one, respectively.

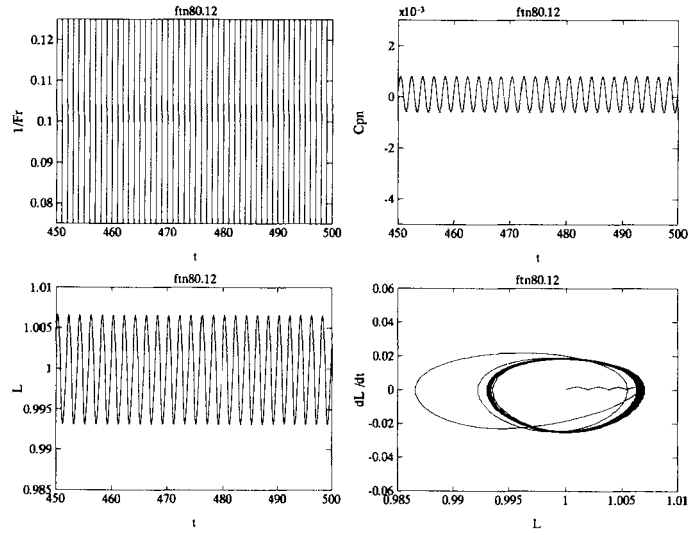

Figure 15. Inverse of the Froude number (top left), pressure coefficient (top right), convergence length (bottom left) and phase diagram for the convergence length (bottom right) as functions of time ($a = 0{\cdot}25$, $S = 0{\cdot}1$, pulse width = 1, time between pulses = 0)

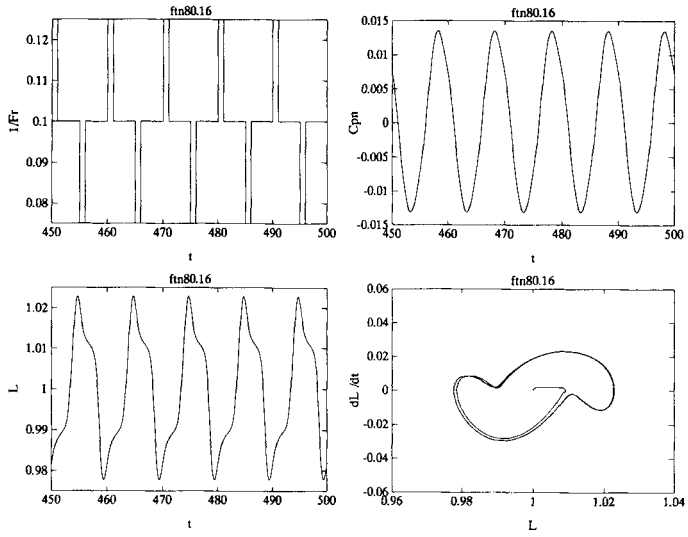

Figure 16. Inverse of the Froude number (top left), pressure coefficient (top right), convergence length (bottom left) and phase diagram for the convergence length (bottom right) as functions of time ($a = 0{\cdot}25$, $S = 0{\cdot}1$, pulse width = 1, time between pulses = 4)

The effects of the width of the rectangular, gravitational fluctuations of $a = 0{\cdot}25$ and $S = 0{\cdot}1$ are illustrated in Figures 18–20 which indicate that the amplitude of both the pressure coefficient and the convergence length are nearly independent, but suffer large changes, as the width of the gravitational pulses is increased. The number of small loops and the shape of the phase diagrams for the convergence length increase and undergo large changes, respectively, as the pulse width is increased.

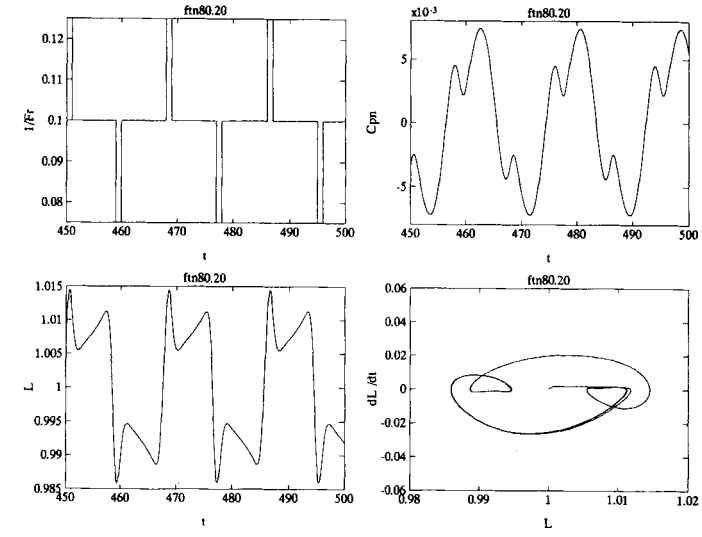

Figure 17. Inverse of the Froude number (top left), pressure coefficient (top right), convergence length (bottom left) and phase diagram for the convergence length (bottom right) as functions of time ($a = 0{\cdot}25$, $S = 0{\cdot}1$, pulse width = 1, time between pulses = 8)

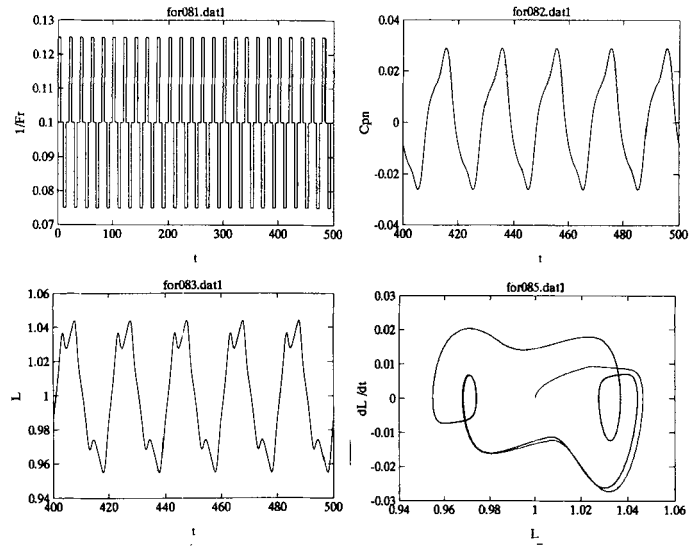

Figure 18. Inverse of the Froude number (top left), pressure coefficient (top right), convergence length (bottom left) and phase diagram for the convergence length (bottom right) as functions of time ($a = 0{\cdot}25$, $S = 0{\cdot}1$, pulse width = time between pulses = 5)

Figures 12–20 also indicate that the maxima and minima of the pressure coefficient occur approximately at the times when the inverse of the Froude number reaches its average value, while those of the convergence length are located at, approximately, the times when the inverse of the Froude number reaches its maximum and minimum values. Similar trends to those shown in Figures 12–20 have been observed for sinusoidal, gravitational modulations, and are not presented here.

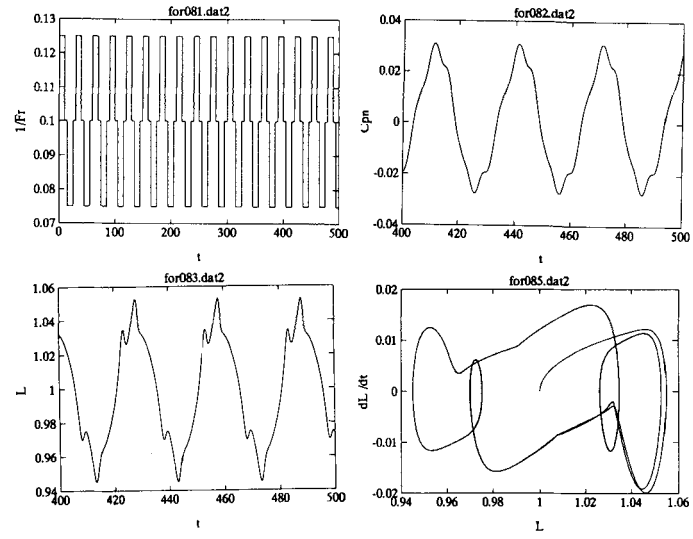

Figure 19. Inverse of the Froude number (top left), pressure coefficient (top right), convergence length (bottom left) and phase diagram for the convergence length (bottom right) as functions of time ($a = 0{\cdot}25$, $S = 0{\cdot}1$, pulse width = 5, time between pulses = 10)

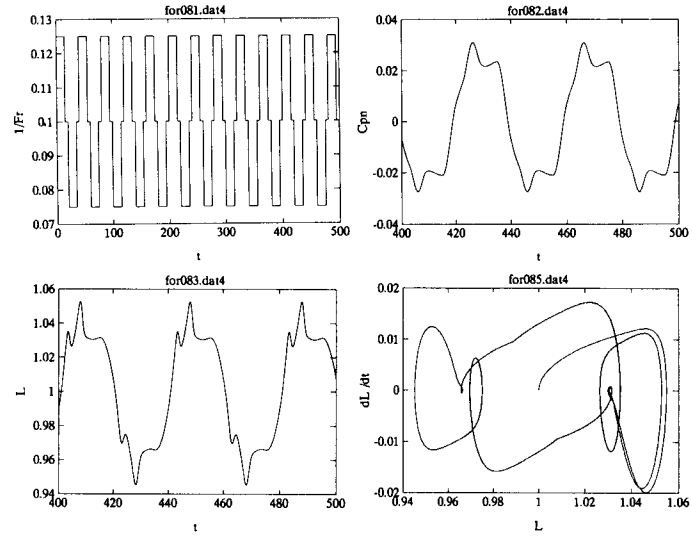

Figure 20. Inverse of the Froude number (top left), pressure coefficient (top right), convergence length (bottom left) and phase diagram for the convergent length (bottom right) as functions of time ($a = 0{\cdot}25$, $S = 0{\cdot}1$, pulse width = 5, time between pulses = 15)

7. CONCLUSIONS

Perturbation methods have been used to derive the asymptotic, one-dimensional equations which govern the fluid dynamics of inviscid, incompressible, irrotational, slender, thin, annular liquid jets from the two-dimensional Euler equations in cylindrical polar co-ordinates using the slenderness and thickness ratios as small parameters. It is shown that, depending on the magnitude of the Weber number two flow regimes may be identified: the inertia-dominated flow regime corresponds to large Weber numbers, whereas the capillary one is associated with Weber numbers of the order of one. The capillary flow regime has also been analysed using the capillary velocity as reference.

For steady, annular liquid jets, it has been shown that the capillary flow regime is characterized by cylindrical, annular jets of a radius proportional to the difference between the pressure of the gases enclosed by and that of those surrounding the liquid, falling under gravity according to Torricelli's free-fall law. The same law is also found to apply to the inertia-dominated flow regime; however, the radius of the jet may not be determined analytically, and a fourth-order accurate Runge–Kutta method was employed to determine the shape of inertia-dominated, annular jets.

Asymptotic methods have also been used to study the governing equations of a previous hydraulic model. It has been shown that this model reduces to those obtained from the Euler equations by means of perturbation methods, and accounts for differences between the pressure of the gases enclosed by and that of those surrounding the liquid even when the Weber number is large enough. However, the one-dimensional models obtained from the Euler equations by means of perturbation methods require that the pressure be uniform throughout the liquid and the gases surrounding and enclosed by the annular jet at high Weber numbers.

The hydraulic model has been used to determine the unsteady fluid dynamics of thin, annular liquid jets subject to gravity modulation, and the results of these studies indicate that both the pressure of the gases enclosed by and the convergence length of the annular liquid jet are periodic functions of time whose amplitude increases as the amplitude of the gravity modulation is increased, is nearly independent of the width of the rectangular, gravitational pulses, and first increases and then decreases

as the separation between pulses is increased. The phase diagram for the convergence length undergoes large changes as the amplitude and width of the rectangular gravitational pulses is increased.

ACKNOWLEDGEMENTS

The research reported in this paper was supported by Project PB91-0767 from the D.G.I.C.Y.T. of Spain. The author is grateful to The Centro Europeo de Paralelismo de Barcelona (CEPBA), Spain, where some of the computations presented here were performed on a CONVEX C3480 supercomputer.

REFERENCES

1. M. Boussinesq, 'Théorie des expériences de Savart, sur la forme que prend une veine liquide après s'être choquée contre un plan circulaire', *Comptes Rendues de l'Académie de Sciences de Paris*, **69**, 45–48 (1869).
2. M. Boussinesq, 'Théorie des expériences de Savart sur la forme que prend une veine liquide après s'être heurtée contre un plan circulaire', *Comptes Rendues de l'Académie de Sciences de Paris*, **69**, 128–131 (1869).
3. G. N. Lance and R. L. Perry, 'Water Bells', *Proceedings of the London Physical Society (London), Series B*, **66**, 1067–1072 (1953).
4. F. L. Hopwood, 'Water Bells', *Proceedings of the Physical Society (London), Series B*, **65**, 2–5 (1952).
5. G. I. Taylor, 'The Dynamics of Thin Sheets of Fluid. Part I–Water Bells', *Proceedings of the Royal Society (London), Series A* **253**, 289–295 (1959).
6. M. H. I. Baird and J. F. Davidson, 'Annular Jets-I. Fluid Dynamics', *Chemical Engineering Science* **17**, 467–472 (1959).
7. A. M. Binnie and H. B. Squire, 'Liquid Jets of Annular Cross-Section', *The Engineer (London)* **171**, 236–238 (1941).
8. J. H. Dumbleton, 'Effect of Gravity on the Shape of Water Bells', *Journal of Applied Physics* **40**, 3950–3954 (1969).
9. M. A. Hoffman, R. K. Takahaski and R. D. Monson, 'Annular Liquid Jet Experiments', *ASME Journal of Fluids Engineering* **102**, 344–349 (1980).
10. J. I. Ramos, 'Liquid Curtains-I. Fluid Mechanics', *Chemical Engineering Science* **43**, 3171–3184 (1988).
11. C. P. Lee and T. G.Wang, 'A Theoretical Model for the Annular Jet Instability', *Physics of Fluids* **29** (7), 2076–2085 (1986).
12. C. P. Lee and T. G.Wang, 'The Theoretical Model for the Annular Jet Instability–Revisited', *Physics of Fluids A: Fluid Dynamics* **1**(6), 967–974 (1989).
13. J. I. Ramos, 'Annular Liquid Jets: Formulation and Steady State Analysis', *Zeitschrift für Angewandte Mathematik und Mechanik (ZAMM)* **72**, 565–589 (1992).
14. J. I. Ramos,'Analytical, Asymptotic and Numerical Studies of Liquid Curtains, and Comparisons with Experimental Data', *Applied Mathematical Modelling* **14**(4), 170–183 (1990).
15. J. I. Ramos, 'Domain-Adaptive Finite Difference Methods for Collapsing Annular Liquid Jets', *Computational Mechanics: An International Journal* **11**(1), 28–64 (1993).